Available online at www.sciencedirect.com
ScienceDirect
Journal of Electroanalytical Chemistry 597 (2006) 1–12
Journal of Electroanalytical Chemistry
www.elsevier.com/locate/jelechem

Surface termination and hydrogen bubble adhesion on Si(1 0 0) surfaces during anisotropic dissolution in aqueous KOH

Wolfgang Haiss [a,*], Philipp Raisch [a], Lennart Bitsch [a], Richard J. Nichols [a], Xinghua Xia [b], John J. Kelly [b], David J. Schiffrin [a]

[a] University of Liverpool, Chemistry Department, Crown Street, Liverpool L69 7ZD, UK
[b] Debye Institute, Utrecht University, P.O. Box 80000, 3508 TA Utrecht, Netherlands

Received 17 October 2005; received in revised form 16 May 2006; accepted 24 July 2006
Available online 18 September 2006

Abstract

The formation and growth of hydrogen bubbles on a Si(1 0 0) surface during its anisotropic etching in aqueous KOH has been investigated. Quantitative data on bubble size, lifetime and density on the etching surface was obtained and their dependence on KOH concentration, applied potential and temperature were measured. *In situ* FTIR measurements demonstrated a strong dependence of bubble attachment on surface termination and hence on the hydrophilicity of the Si(1 0 0) surface during etching. The formation of surface defects and the geometry of bubble imprints have been directly characterised with scanning probe microscopy. The analysis of hillock formation and statistical considerations show that the adhesion of hydrogen bubbles during anisotropic etching of silicon is a source of surface roughness and pyramid formation.
© 2006 Elsevier B.V. All rights reserved.

Keywords: Silicon etching; Bubble adhesion; Micromachining; Anisotropic etching; FTIR spectroscopy; Si(1 0 0); Hillock formation

1. Introduction

Etching of silicon in alkaline solutions is widely employed in micromachining [1,2]. Beams and membranes for mechanical sensors and actuators [3,4], V-groove structures used for the passive alignment of glass fibres in optoelectronic devices and complex micro-electromechanical systems (MEMS) [5,6] can be easily fabricated using the anisotropic dissolution of single crystal silicon [7,8]. Modern exacting demands [9] require the production of defect-free structures with a well-defined anisotropic ratio and high quality surface finish with surface features of nanometer dimension. For this reason it is important to elucidate the mechanism of formation of micro-pyramids and of large-scale roughness during the wet chemical etching of silicon.

Two hydrogen molecules are released for each silicon atom dissolved [10] and $Si(OH)_4$ is regarded as the primary reaction product [11,12]. The overall reaction is [13,14]

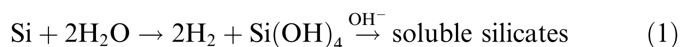

$$Si + 2H_2O \rightarrow 2H_2 + Si(OH)_4 \overset{OH^-}{\rightarrow} \text{soluble silicates} \quad (1)$$

Etching defects and surface roughness can result if the hydrogen bubbles produced remain long enough on the surface to mask it from the etching solution [15–19]. The purpose of this work was to investigate the physicochemical aspects of bubble adhesion from measurements of bubble size, lifetime and IR spectroscopy of Si(1 0 0) surfaces in contact with aqueous KOH. In addition, scanning probe techniques have been used to elucidate the role of bubbles in the formation of surface defects (i.e. micro-pyramids) and/or large-scale surface roughness during etching.

* Corresponding author. Tel.: +44 1517943556; fax: +44 1517943588.
E-mail address: w.h.haiss@liv.ac.uk (W. Haiss).

0022-0728/$ - see front matter © 2006 Elsevier B.V. All rights reserved.
doi:10.1016/j.jelechem.2006.07.027

2. Experimental methods

2.1. Chemicals and samples

Unless otherwise stated, samples were Czochralski grown, phosphorous doped n-Si(100) wafers (1–20 Ω cm; orientation tolerance ±2°; Compart Technology, UK) or boron-doped p-Si(100) wafers (1–30 Ω cm; orientation tolerance ±0.5°; Okmetic, Finland). The silicon working-electrode was mounted in a Kel-F holder and the exposed surface limited with an "o"-ring. Electrical contact was made to the backside of the sample with Ga/In eutectic. Milli-Q water and analytical grade KOH (Fluka puriss p.a.) were used throughout. As described below, different procedures were used to remove the native oxide, depending on the type of measurement performed.

2.2. Voltammetry and etch rate measurements

For these measurements, the native oxide was removed before each measurement by dipping the wafers in 1 M HF + 2 M NH_4F (Merck, p.a.) for 1 min followed by rinsing with water. The electrochemical experiments were carried out with a PAR 283 potentiostat (EG&G Princeton Applied Research) controlled by a personal computer via a LabVIEW interface (National Instruments). The current–potential scans (voltammograms) were measured in the dark and the potential was scanned from negative to positive values at a scan rate of 1 mV/s. The etch rate was determined by measuring the etched depth as a function of etching time using a surface profiler (Dektak II, Veeco Instruments).

2.3. Video microscopy

The samples were rinsed first in ethanol and then in water and finally blown dry in argon (Pure shield, BOC) before mounting on the sample holder. A circular area of 0.95 cm^2 was exposed to the solution. The etching solutions were not deaereated. The native oxide was stripped directly in the etching solution at 60 °C. This procedure avoided excessive roughening of the surface at the beginning of etching, which was observed for HF-dipped samples. Etching was carried out in a 200 cm^3 Pyrex glass vessel equipped with an optical flat. The sample was illuminated from the side with a slide projector. The potential of the silicon surface was controlled with a home-built potentiostat and the temperature was kept constant with a PYE UNICAM temperature controller. A television camera (MK 11 Series Tube Camera; DAGE-MTI, Inc.) in conjunction with a Nikon objective (Micro-Nicor, 105 mm; f/4) was used to image the surface. The images were displayed on a television monitor with a ×15 magnification factor, stored in a Toshiba V-858B video recorder and subsequently analysed on a PC using a commercial frame grabber (All-In-Wonder 128 AGP 16 MB; ATI Technologies, Inc.). The lifetime (τ) of the hydrogen bubbles on the surface (i.e. the time between initial formation and detachment) was determined from the video images using a stopwatch. For lifetimes shorter than 1 s the number of video frames for which the bubble was visible were counted, resulting in this case in a time resolution of 40 ms (±1 frame). Bubble diameters were measured directly from the frozen video frame on the computer screen before detachment of the bubbles took place. With this simple method the bubble diameter (d) was determined with an accuracy of ±0.02 mm. The screen was calibrated using the sample holder as an internal standard.

2.4. Scanning probe techniques

In contrast with the video microscopy experiments, the native silicon oxide layer was removed prior to etching by immersion in 2 M HF (Fluka puriss p.a.) for 2 min to ensure that etching commenced immediately after immersion in the KOH solution. After the HF dip the samples were rinsed with water and blown dry in a stream of argon (Pure Shield, BOC). Samples were etched whilst lying horizontally at the bottom of a glass vessel filled with 2 M KOH. The etching was performed in the dark at room temperature and no sample holder was used. At the end of the etch period, the samples were rinsed in water for 30 s and subsequently immersed in 0.8 M sulphuric acid for 5 min to remove any residual KOH. This was followed by another 2 min water rinse. The samples were finally blown dry in a stream of argon. A surface profiler (Dektak II, Veeco Instruments) was used to characterise the long-range defects (imprints) caused by hydrogen bubbles during the early stages of etching. The radius of the diamond tip used was 1 μm. A Molecular Imaging PicoScan atomic force microscope was employed for *ex situ* AFM imaging as previously described [20]. The surface of the etched samples was examined with a Philips XL30FEG scanning electron microscope.

2.5. FTIR spectroscopy

FTIR spectroscopy measurements were carried out in the attenuated total reflectance (ATR) configuration [21]. Prisms were made from float zone grown Si(100) wafers (1 kΩ cm, Compart Technology, UK). All FTIR measurements were carried out at room temperature. Both a Bruker IFS 66v/S and a Bio-Rad FTS-40 infrared spectrometer were employed. The potential was controlled with a potentiostat (DT2101, Hi-Tek Instruments, UK). The counter electrode was a platinum mesh and an oxidised Ag wire was used as a pseudo reference electrode. This electrode was calibrated with respect to a saturated calomel electrode (SCE) and all potentials are referred to the SCE scale. Infrared absorption spectra were acquired using the SNIFTIRS (Subtractively Normalised Interfacial FTIR Spectroscopy) technique [22]. Briefly, successive series of interferograms were collected at the reference potential E_1 and at the sample potential E_2. The relative change in transmitted IR intensity is given by

$$\frac{\Delta I}{I} = \frac{I(E_1) - I(E_2)}{I(E_1)} \quad (2)$$

where I_1 and I_2 are the infrared intensities transmitted through the silicon crystal at the potentials E_1 and E_2. With this convention an upward (positive) going band corresponds to greater spectral absorbance of the sample at E_2. For the measurements at steady-state conditions a time of 60 s was allowed to elapse between acquisition of spectra at E_1 and E_2. All spectra were corrected to remove sloping baselines [21].

The ATR prisms were polished with diamond paste (0.05 μm) and then rinsed with ethanol and water. For the *in situ* experiments, the ATR prism was not etched with HF to eliminate the native oxide since this treatment, followed by contact with aqueous KOH, led to large surface roughness and substantial loss of the IR signal. Instead, the polished and rinsed prism was immersed directly in the KOH solution under study and smooth surfaces were obtained after etching approximately 1 μm of the surface at a potential of −1 V. This preparation method ensured that the crystal did not roughen during the initial etching, an important consideration for the KOH solutions of lower concentration.

3. Results and discussion

3.1. Voltammetry and etch rate measurements

The dissolution of Si(1 0 0) in aqueous KOH is a complex process in which two mechanisms are involved [23–25]. In the chemical mechanism silicon is dissolved in a hydroxide-catalysed, thermally activated chemical reaction, in which water is the reactive species. Simultaneously with this, an electrochemical dissolution pathway may take place. Most of the silicon dissolves by the chemical dissolution pathway.

Fig. 1 compares voltammograms of p- and n-Si(1 0 0) in 2 M KOH at 70 °C with the etch rates measured at different potentials. The general features of the current–potential curves measured at other temperatures (20–70 °C) and KOH concentrations (2–10 M) were similar to those shown in Fig. 1 and to results described in the literature [12,26–29]. At potentials positive of the open circuit potential (OCP), a pronounced increase of current is observed that reaches a maximum at E_p and finally drops sharply to low values. The strong drop of the current is associated with the formation of a surface oxide [10,14,29–31] and consequently, the rapid drop in the etch rate to zero is due to anodic passivation. At potentials negative of the OCP a negative current is observed for n-Si(1 0 0) due to the hydrogen evolution reaction proceeding under accumulation conditions. No current flow is observed for p-Si(1 0 0) in this potential range in the dark since the surface is depleted. The very large decrease in the etch rate observed for n-Si in the potential range from −1.3 to −2 V is due to a significant change in the Helmholtz potential [32]. This change does not take place for p-Si since it is under depletion conditions in this potential range and therefore a constant etch rate is observed for this material.

3.2. Size and lifetime of attached bubbles

Fig. 2 shows the influence of potential on bubble size and number density for n-Si(1 0 0) etched in 2 M KOH at 71 °C. Bubble nucleation occurs randomly over the surface and the average size and density of attached hydrogen bubbles increases as the potential is changed from −1.07 V (Fig. 2a) to −1.17 V (Fig. 2b). A drastic increase of bubble size is observed at more negative potentials (−1.63 V, Fig. 2c). At even more negative potentials ($E = -2$ V, Fig. 2d), the surface ceases to etch (see Fig. 1b) and electrochemical hydrogen evolution takes place at specific sites.

Fig. 3 shows images of p-Si(1 0 0) during etching in KOH under various conditions to illustrate the influence of KOH concentration (c_{KOH}), temperature and potential on bubble adhesion. At high KOH concentration and at anodic potentials (Fig. 3a) only a few bubbles are visible on the surface due to their rapid detachment and their small size compared with those observed at more negative potentials (compare Fig. 3a at −0.90 V with Fig. 3b at −1.27 V) indicating a stronger adhesion of bubbles to the surface as the potential is made more negative. An increase in temperature does not change significantly the average size of the

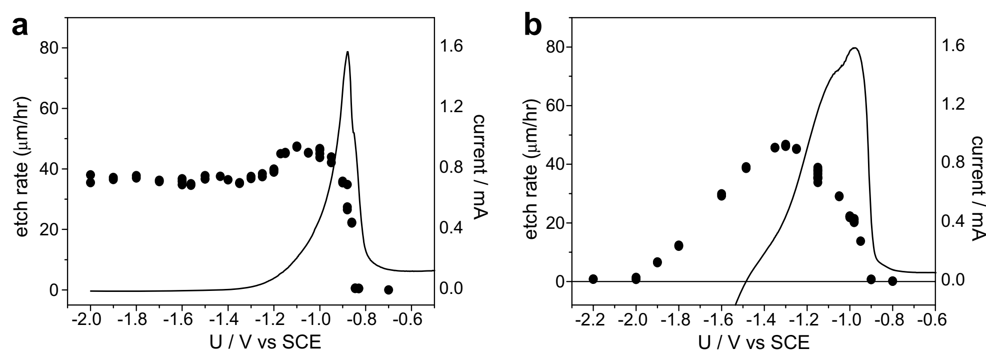

Fig. 1. Dependence of the etch rate of p-type (a) and n-type (b) silicon on potential in 2 M KOH solution at 70 °C (circles). The current–potential curves for each type of silicon under the same conditions are shown for comparison (solid lines).

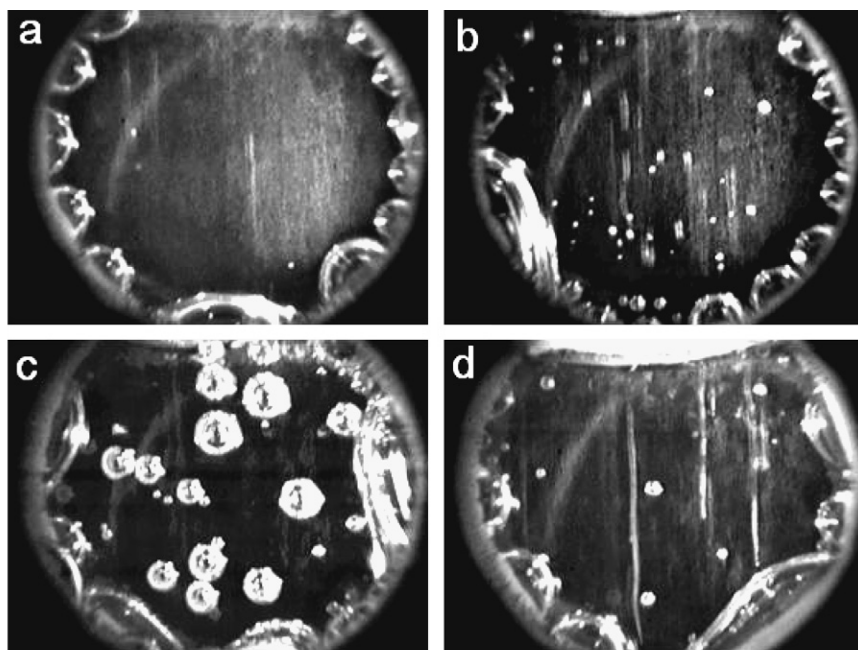

Fig. 2. Potential dependence of bubble formation on n-Si(1 0 0) in 2 M KOH sample holder diameter = 1.13 cm; (a) $E = -1.07$ V (current maximum); only a few small bubbles are adhering to the surface for a very short time and most of the hydrogen is nucleating at the sample holder edge. (b) $E = -1.17$ V; bubble size and density is increasing compared to (a). (c) $E = -1.63$ V; the size of the bubbles increases dramatically. (d) $E = -2.0$ V; the nucleation of bubbles takes place mainly at specific surface sites. At this potential the surface is no longer etching and direct electrochemical evolution of hydrogen is observed (compare with Fig. 1(b)). $T = 71$ °C.

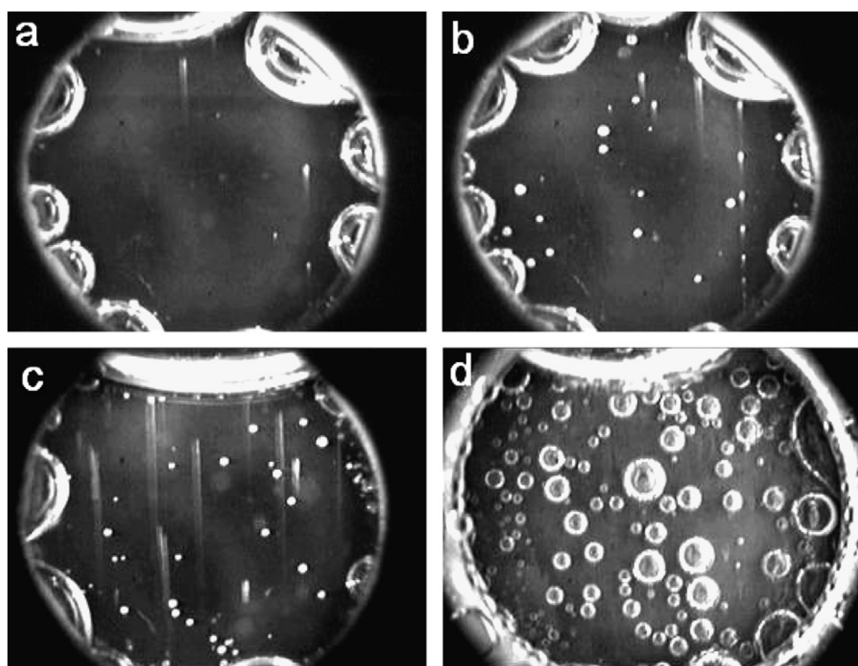

Fig. 3. Bubble formation on p-Si(1 0 0) during etching in KOH under various conditions. Sample holder diameter = 1.13 cm. (a) 6 M KOH; $E = -0.9$ V; $T = 23$ °C; (b) 6 M KOH; $E = -1.27$ V; $T = 23$ °C; (c) 6 M KOH; $E = -1.27$ V; $T = 51$ °C. The increase of temperature decreases the average bubble size marginally but more bubbles are formed due to an increase of etch rate (compare with (b)). (d) 2 M KOH; $E = -1.23$ V; $T = 51$ °C. The bubble lifetime and the average bubble size increases dramatically at lower KOH concentrations (compare with (c)).

bubbles (compare Fig. 3b and c), but a decrease of c_{KOH} from 6 to 2 M increases the average size by an order of magnitude (compare Fig. 3c and d). Figs. 2 and 3 clearly demonstrate that the average bubble size is strongly dependant on E and c_{KOH}. This dependence was found to be qualitatively similar in the potential region positive to the

anodic peak for n- and p-Si, whereas the differences mentioned above are observed at potentials negative of the OCP.

The dependence of bubble diameter (d) on bubble lifetime (τ) is shown in Fig. 4. The average diameter for a sequence of 35 bubbles and their lifetime is shown as an open circle in this figure. It was observed that the formation and detachment of bubbles on the surface is a random process. Bubbles do not emerge at special sites but their formation is distributed evenly over the whole area and bubble lifetime shows a broad distribution. The experimentally observed relation between bubble diameter and the bubble lifetime in Fig. 4 can be described by

$$d(\tau) = a(T)\tau^{1/2} \tag{3}$$

where the coefficient a depends on temperature. This representation is consistent with a bubble growth model proposed by Scriven, which relates radial mass transfer to spherical phase growth controlled by diffusion [33]. This model leads to [34]

$$d = 4\beta(kt)^{1/2} \tag{4}$$

where β is a dimensionless growth parameter and k is the temperature-dependent diffusivity.

Fig. 5a shows the potential dependence of the average lifetime of hydrogen bubbles on p-Si(100) in 2 M KOH. Remarkably, a change of potential from −1.2 to −0.85 V reduces τ by two orders of magnitude. The average diameter d scales approximately with $\tau^{1/2}$, independently of potential (Fig. 5b). Fig. 6 shows similar measurements on n-Si(100). A potential change from −1.63 to −1.07 V decreases the bubble size by approximately an order of magnitude and the bubble lifetime by two orders of magnitude. The pronounced influence of KOH concentration on bubble lifetime, measured at the OCP, is also shown in this figure; an increase in KOH concentration from 1.7 to 6 M decreases τ by nearly two orders of magnitude.

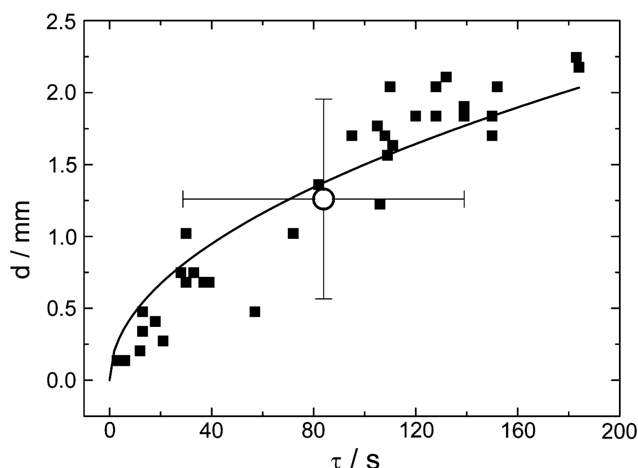

Fig. 4. Dependence of the lifetime (τ) of 35 different hydrogen bubbles formed during etching of n-Si(100) in 1.7 M KOH at 24 °C on their diameter d (solid squares). The solid line shows a non-linear regression fit ($d = 0.15t^{1/2}$). The open circle represents the average of the data and the error bars represent the standard deviation.

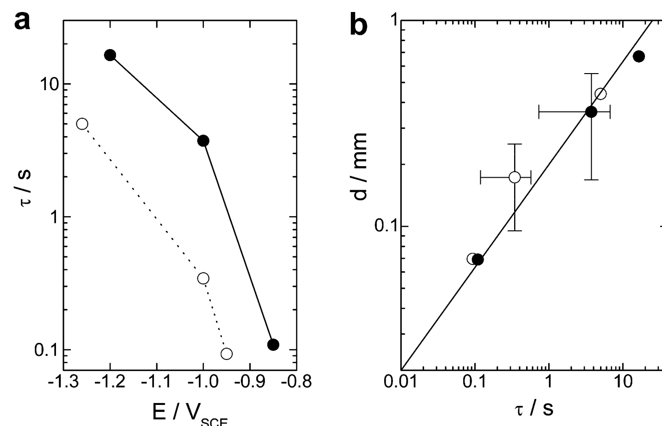

Fig. 5. (a) Potential dependence of the average lifetime (τ) of hydrogen bubbles on p-Si(100) formed during etching in 2 M KOH at 74 °C (open circles) and 52 °C (filled circles). (b) Average lifetime (τ) of bubbles from (a), plotted against their average diameter (d). Error bars represent the standard deviation.

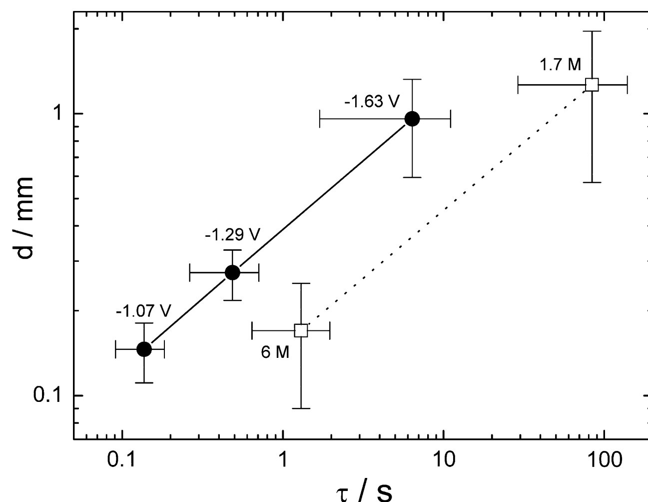

Fig. 6. Dependence of the average lifetime (τ) of hydrogen bubbles on n-Si(100) formed during etching in 2 M KOH at 71 °C on their average diameter (d) for different potentials (solid circles). The room temperature measurements show the influence of KOH concentration on bubble size and lifetime (open squares). The number next to the symbols represents the potential at which each data point was measured. Error bars represent the standard deviation.

3.3. Surface morphology

Fig. 7 shows typical profile scans through the centre of circular bubble imprints observed on n-Si(100) etched only for a few minutes in 2 M KOH. In these measurements, the exposure time to the solution was small to avoid interference from excessive surface roughness. The profiles observed are strongly dependent on d_c, the diameter of the circular region where the surface is not in direct contact with the solution. Small bubbles ($d_c \approx 20$ μm) result in

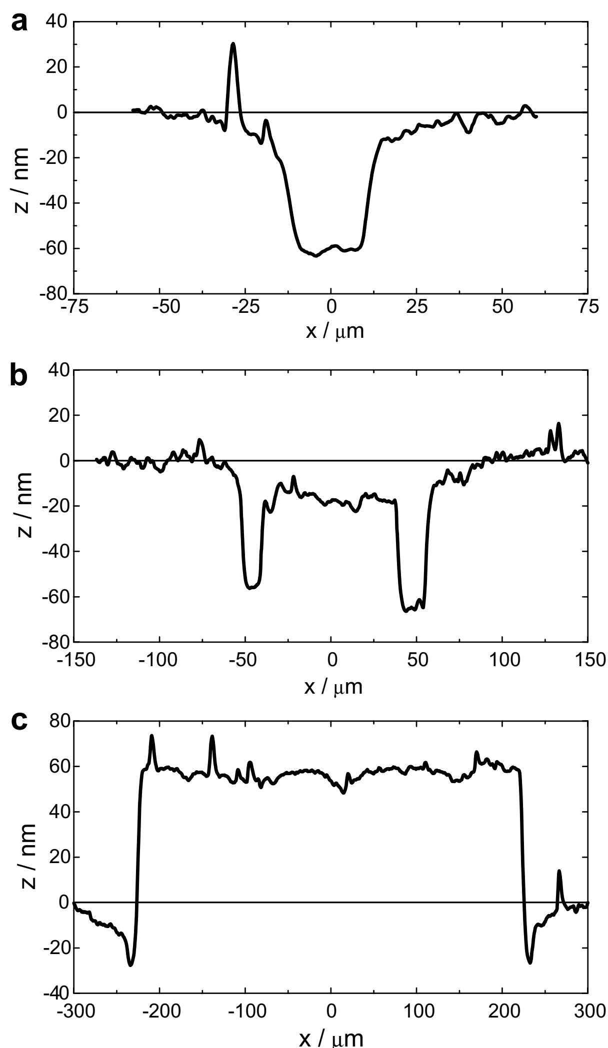

Fig. 7. Line scans through the centre of circular bubble imprints observed on n-Si(100) after etching in 2 M KOH for 8 min at room temperature. Small bubbles result in depressions (a) whereas large bubbles result in the formation of plateaux (c). At an intermediate bubble diameter a situation is encountered in which a circular trench is observed on the sample (b).

depressions (Fig. 7a), medium size bubbles ($d_c \approx 100$ μm) create circular trenches (Fig. 7b), whereas large bubbles ($d_c > 100$ μm) result in circular plateaux (Fig. 7c). The height of these plateaux increases with their diameter and hence they can be attributed to a macroscopic masking effect.

To explain these findings it is instructive to consider a simple bubble growth model as it is schematically shown in Fig. 8. A diffusion layer surrounds the hydrogen bubble during its expansion phase. A thin, circular film of liquid with a thickness of 1–100 nm is formed in the vicinity of the three-phase boundary solid–liquid–gas. The concentration of KOH in this thin film is expected to increase rapidly due to water decomposition and hence the chemical and/or electrochemical properties of the solid–liquid interface in the thin film region are different from those of the surrounding media, resulting in an increased etch rate at the three-phase boundary. This explains the observation of holes and circular trenches in the early stages of bubble growth (see Fig. 7a and b). A local increase of potential and/or KOH concentration can also explain the observation of reduced roughness within holes and circular trenches (Fig. 7) when etching at this thin film takes place. At a later stage of bubble growth ($d > 100$ μm) the masking effect of the bubbles is dominant and circular plateaux are observed (Fig. 7c). Fig. 8c summarises schematically the different types of bubble imprints. The height of the surface is represented by different grey-levels where darker areas represent depressions and lighter areas represent protrusions. Small

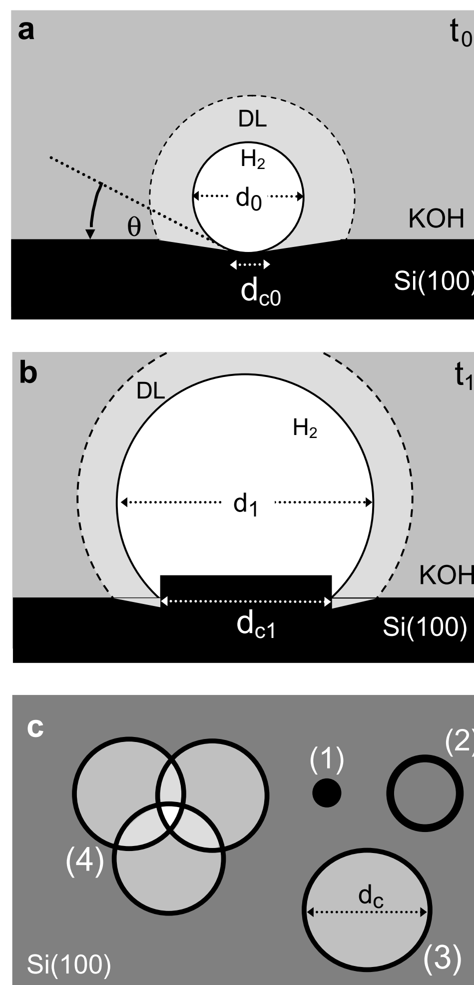

Fig. 8. (a) Schematic representation of the growth of a hydrogen bubble on n-Si(100) in 2 M KOH. The bubble is formed by H_2 diffusion from the liquid (DL = Diffusion Layer). The formation of a depression in the etching surface is observed during initial bubble growth where the properties of a thin solution film at the three-phase boundary solid–liquid–gas are dominant. (b) Geometry at a later stage of bubble growth where the masking effect due to bubble adhesion to the Si surface can be clearly observed. Note that $\theta^* = 180° - \theta_c$ where θ_c is the contact angle. (c) Schematic top view of the surface after bubble removal. Bubble imprints depend on the size of the bubble which caused them: small bubbles result in depressions (1), medium size bubbles in rings (2) and large bubbles in plateaux (3). Overlapping plateaux result in particularly tall protrusions (4).

bubbles result in depressions (Fig. 8c(1)), medium size bubbles result in rings (Fig. 8c(2)), large bubbles result in plateaux (Fig. 8c(3)) and overlapping plateaux result in particularly tall protrusions (Fig. 8c(4)).

The dependence of topography of n-Si(100) on etching time was monitored by AFM and representative results are shown in Fig. 9. Before a steady state is reached, after approximately 90 min, pyramidal protrusions grow at a rate similar to the etch rate of the surrounding (100) plane [20]. At the OCP, the number density of these micro-pyramids decreases with increasing pyramid height and after approximately 90 min, the pyramids cease to grow. The microscopic structure of the Si(100) surface exhibits a strong dependence on both E and c_{KOH}. Fig. 10 shows scanning electron microscopy images of a n-Si(100) surface taken after 30 min of etching at 70 °C in 2 M KOH at −1.7 (a), −0.98 (b) and −2.2 V (c). Roughening developed at

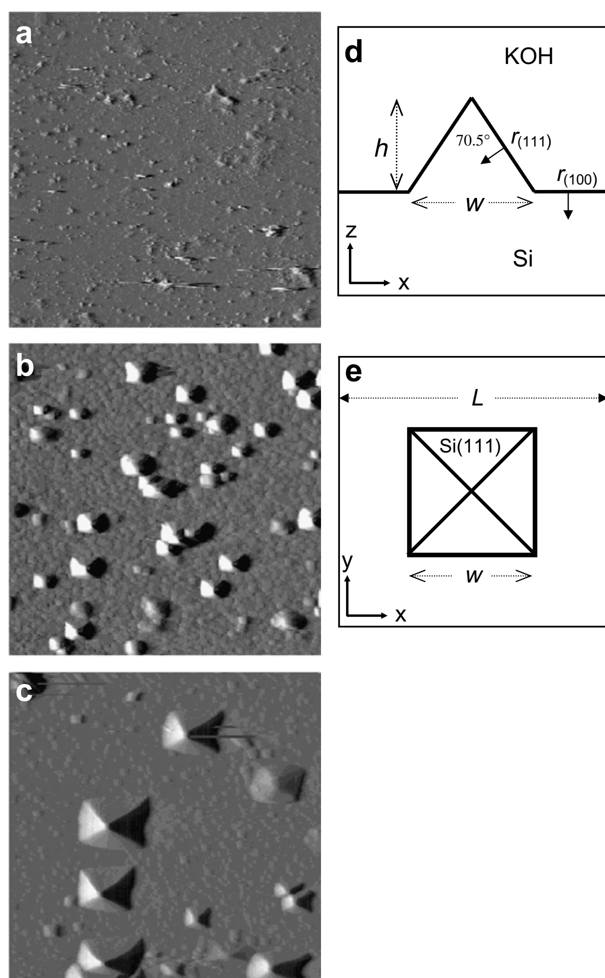

Fig. 9. AFM images of n-Si(100) after etching in 2 M KOH at room temperature for $t = 2$ (a), 40 (b) and 70 min (c); the image size is 15 × 15 μm and schematic model of the surface macroscopic unit cell of Si(100) during etching in KOH. The square unit cell with a size of L^2 contains areas of flat Si(100) surface and a micro-pyramid, delimited by four Si(111) planes with height h and width w. The effective etch rates $r_{(100)}$ and $r_{(111)}$ are symbolised by arrows; (d) side view; (e) top view.

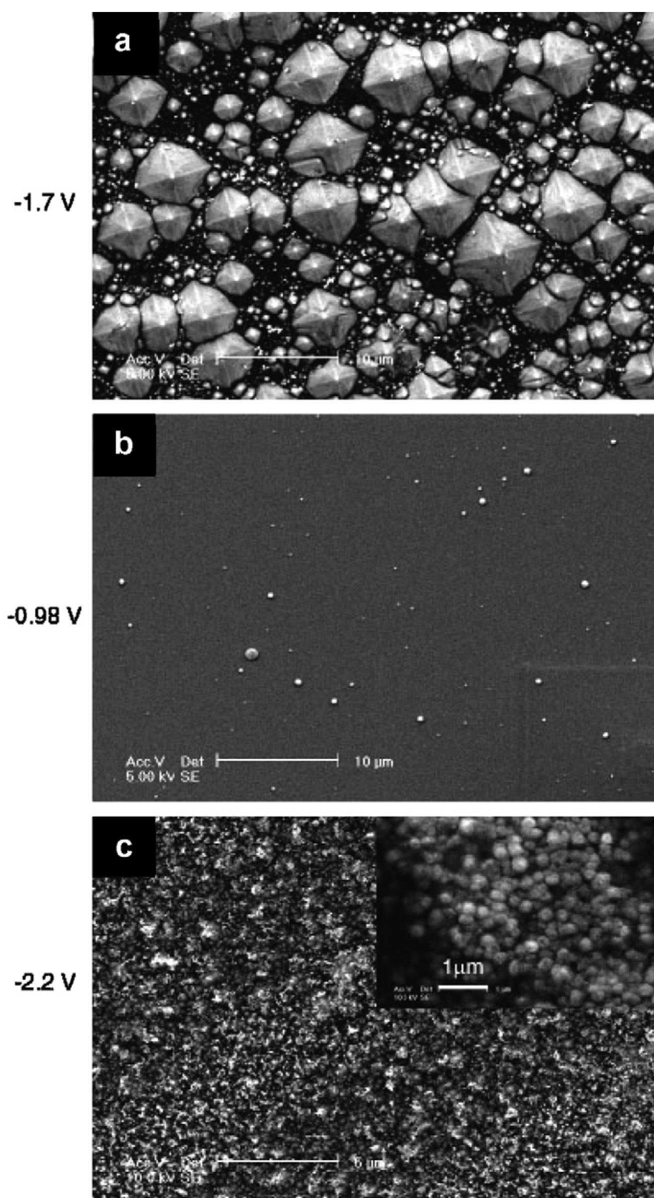

Fig. 10. Scanning electron microscope images of n-Si(100) taken after 30 min of etching in 2 M KOH at 70 °C; $E = -1.7$ (a) −0.98 (b) and −2.2 V (c).

negative potentials whereas during etching at more positive potentials, close to the voltammetric current peak (Fig. 1), almost no defect formation can be observed. These results clearly relate to the bubble adhesion observations. Defect-free etching can also be realised at high KOH concentrations. Table 1 compares values of surface roughness of n-Si(100) after etching in 2 and 6 M KOH showing that steady-state roughness is observed for all materials after approximately 1 h of etching.

3.4. Surface termination and bubble adhesion

Fig. 11 shows in situ SNIFTIRS spectra of n-Si(100) during etching in 6 M KOH. The spectra shown are limited

Table 1
Root mean square roughness (R_q) for n-Si(100) etched at room temperature in aqueous KOH at the OCP

c_{KOH}/mol dm^{-3}	t_{etch}/h	R_q/nm
2	1	15–100
2	20	800–1200
2	80	850–1300
6	1	3–12
6	20	3–20
6	80	3–25

No HF dip was used before etching but the native oxide was stripped in hot KOH. A root mean square roughness of 1–2 nm was measured on the wafer before etching.

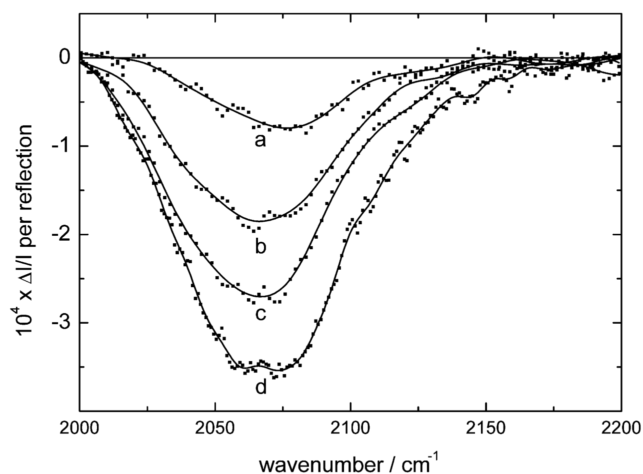

Fig. 11. SNIFTIRS spectra of n-Si(100) in 6 M KOH recorded for potentials (E_2) chosen at successive values in the anodic peak region: (a) −0.95, (b) −0.8, (c) −0.75 and (d) +4.0 V. These spectra are referenced with respect to the spectrum recorded at the OCP (E_1). The negative going bands therefore correspond to the loss of hydrogen coverage when the potential is shifted from the OCP into the anodic peak region.

to the Si–H vibrations region [35–39]. These spectra are referenced to the OCP ($E_1 = -1.59$ V) and the results shown correspond to increasing positive potentials. The downward going bands show that hydrogen is gradually removed from the surface as the potential is made more positive than the OCP. Since all surface hydrogen is removed at $E_2 = +4$ V (spectrum d in Fig. 11) [21], the potential dependence of the integrated band intensity relative to hydrogen coverage at the OCP can be calculated. The results of these calculations together with the observed current are shown in Fig. 12. These data show that for both n-Si(100) (Fig. 12a) and p-Si(100) (Fig. 12b) the coverage by surface hydrogen strongly decreases in the vicinity of the anodic current peak.

SNIFTIRS spectra referenced against the completely oxidised surface, i.e. when no surface hydrogen is present, were also measured at the OCP to study the influence of KOH concentration on surface termination. The results are shown in Fig. 13 as difference spectra of n-Si(100) in contact with 2 and 6 M KOH (dashed and dotted lines respectively). These spectra are compared with that taken in air after the crystal was dipped in HF for 5 min (solid line). The latter surface is expected to be mainly Si–H_2 terminated [35,36] and the maximum of the IR absorption band is therefore expected at 2108 cm^{-1} [40–42], in agreement with the experimental findings (solid line in Fig. 13). Upon immersion of this surface into 2 M KOH at the OCP, the hydrogen coverage is reduced and the IR peak (dashed line in Fig. 13) is shifted to lower wave numbers. This is attributed to the formation of H–Si–O species on the etching silicon surface [21]. A further increase of KOH concentration to 6 M results in a further reduction of the hydrogen coverage and a concomitant shift of the peak maximum to approximately 2060 cm^{-1}. This is an

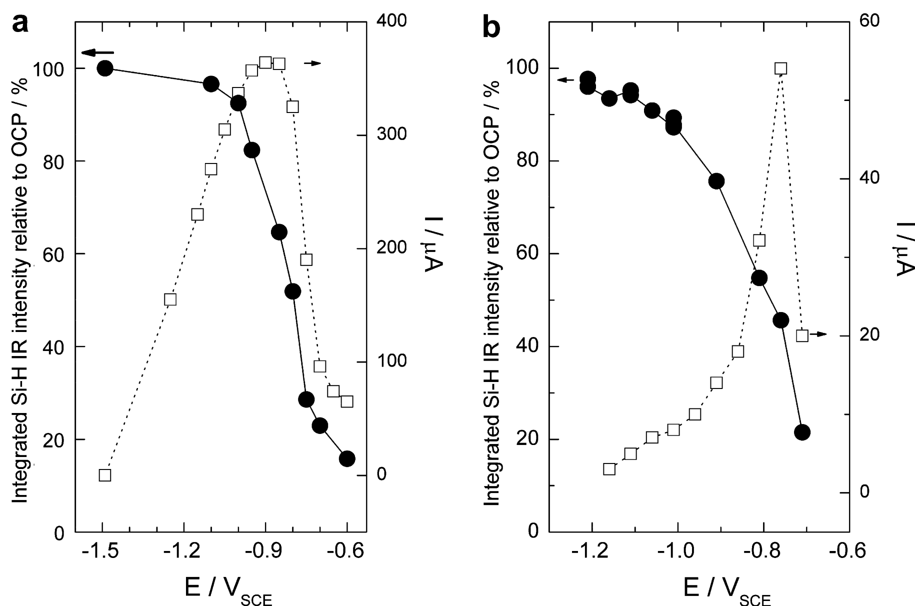

Fig. 12. Normalised integrated IR intensity relative to the OCP of the Si–H absorption band as a function of the potential E_2 for n-Si(100) (a) and p-Si(100) (b) in 6.0 M KOH (filled circles) and the simultaneously recorded steady-state current (open squares).

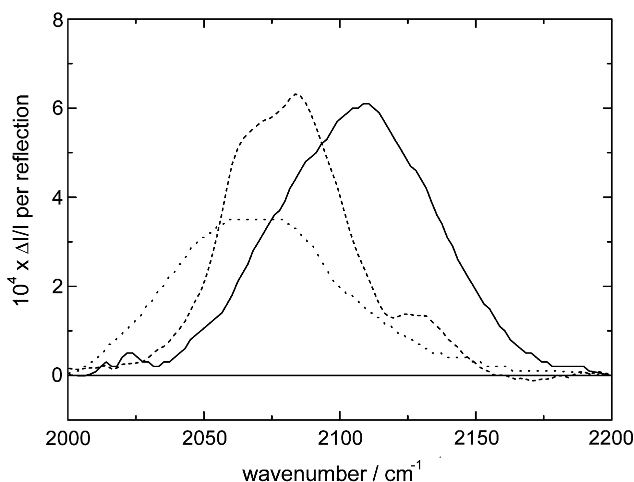

Fig. 13. Infrared absorption spectra of the Si–H vibration band of n-Si(100) during etching in 6 M KOH at the OCP (dotted line), during etching in 2 M KOH at the OCP (dashed line) and for a hydrogen-terminated surface directly after a HF dip (solid line). All three spectra are referenced against the completely oxidised surface.

important observation indicating that the nature of the surface termination changes as the KOH concentration increases, leading to a more hydrophilic surface. The increase in c_{KOH} removes monohydride (2080 cm^{-1}), dihydride (2108 cm^{-1}) and trihydride species (2130 cm^{-1}) from the Si(100) surface whereas a new species (2060 cm^{-1}) is formed. The same changes take place in 2 M KOH when the potential is made more positive, from −1.5 to −0.95 V. It is concluded that the changes in surface species as the potential is made more positive are similar to the changes observed when the c_{KOH} is increased.

For a better understanding of the FTIR spectra, it is instructive to recall the microscopic structure of Si(100) as it is schematically shown in Fig. 14. Silicon has a diamond lattice structure with face centred cubic sub-lattices. When atoms are removed from the (100) surface plane, two different surface sites are exposed. These are denoted as S_1 and S_2 in Fig. 14a. Both sites may exhibit different terminations as depicted in Fig. 14b. In what follows the different sites and terminations will be referred as indicated in this figure. For example, an α_1 site refers to a silicon atom with two back bonds to the lattice and terminated with two hydrogen atoms (a dihydride).

The FTIR spectroscopy results clearly show the presence of three different surface hydrogen species. The band at 2108 cm^{-1}, associated with the dihydride termination (α_1 sites), was observed for HF-dipped samples prior to etching. The absorption at 2080 cm^{-1} is associated with the monohydride (α_2 sites) and is present during etching in 2 M KOH at potentials negative of the OCP, whereas at potentials positive to the OCP the band at 2060 cm^{-1} is related to the H–Si–O$^-$ species (β_1 sites). The results in Fig. 12 demonstrate that the density of α_1 sites on a silicon surface during etching is strongly reduced in comparison to that of a HF-dipped surface, which is terminated with α_1 sites only [35,36]. When the potential is made more positive

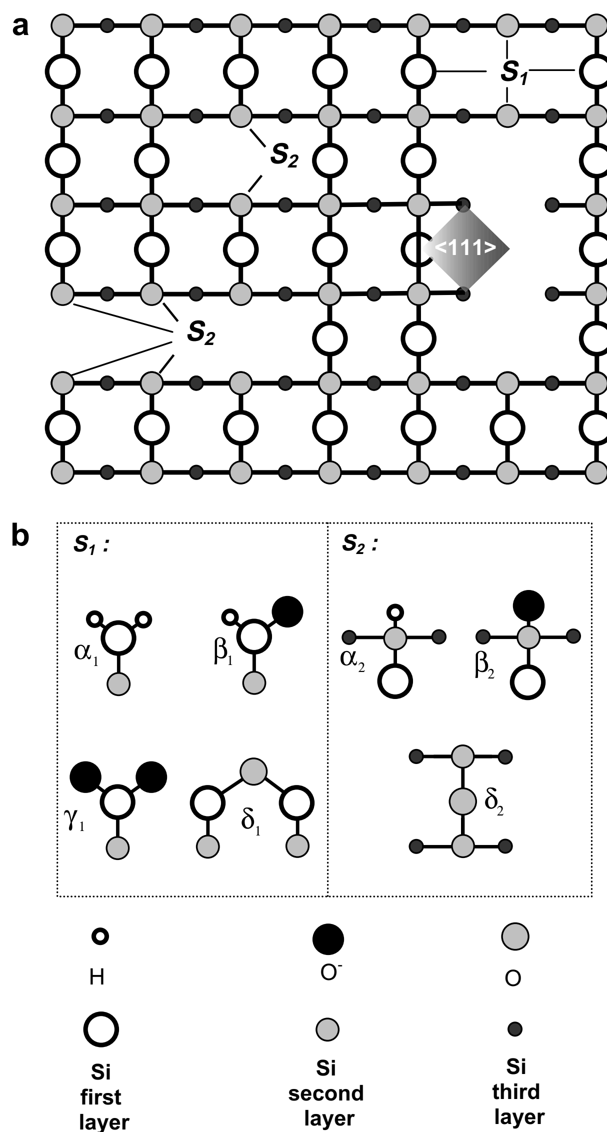

Fig. 14. (a) Schematic top view of a Si(100) surface. The first layer of Si atoms is represented as open circles, the second layer atoms are lightly shaded and those in the third layer are dark. Several silicon atoms have been removed to show the likely sites that are created during etching. S_2 sites have two dangling bonds, while S_1 sites have only one. (b) Several possible surface terminations for the S_1 and S_2 sites.

or the KOH concentration is increased (Figs. 12 and 13), the hydrogen coverage is reduced and new hydrophilic silicon surface species ($\beta_1, \beta_2, \gamma_1$) are formed. The γ sites correspond to dihydroxy terminated Si atoms and the δ sites represent silicon oxide passivated surfaces.

As the potential is made more positive the surface termination changes from hydrophobic to hydrophilic resulting in an increase of surface wettability and a reduction in the contact angle θ (Fig. 8). In consequence, bubble detachment driven by buoyancy effects occurs at an earlier stage of bubble growth since the contact area at bubble detachment is strongly reduced. It is proposed that the changes in surface morphology observed are due to the decrease in bubble lifetime at anodic potentials. The dependence

of bubble adhesion on surface termination is also supported by the observation that bubble lifetime changes in a time scale of seconds after a potential step, as has been reported for changes of the surface termination [21] and photocurrents [43] under similar conditions.

3.5. The origin of surface roughness

Surface roughness in general results from different areas of the surface etching at different rates. Various mechanisms are responsible for this effect, for example the random removal of surface atoms during etching will lead to a roughening of the surface simply due to the statistical nature of this process. This contribution is very small as shown by the small roughness observed after a long etching period in 6 M KOH (see Table 1). It is proposed that this is a consequence of a self-correcting mechanism due to the need to remove four layers of atoms before a (1 1 1) facet is exposed, a rather unlikely process since every second or third layer consists of S_2 sites, which are difficult to attack as compared to the S_1 sites (Fig. 14).

In this paper, we are concerned with the surface roughness occurring as a result of the adhesion of hydrogen bubbles on the etching surface. To decide the likely contribution of this effect, the fraction of exposed (1 1 1) surfaces per unit area ($\sigma_{(111)}$) created by hydrogen bubbles is estimated. For this, it is assumed that the surface area of the rim of a bubble imprint corresponds to the (1 1 1) oriented area created by the bubble. Since the plateaux and the surrounding surface have to be connected with a slow etching surface plane and the stable (1 1 1) surface is the most likely candidate, $\sigma_{(111)}$ can thus be calculated considering the growth rate and the number density of bubble-induced plateaux. This is given by

$$\sigma_{(111)} = L_c r_e t_e \quad (5)$$

with

$$L_c = \pi d \cos\theta_c N \quad (6)$$

L_c denotes the total length of all the contact area perimeters of hydrogen bubbles present on a unit surface area, t_e is the duration of etching, r_e is the average etch rate and N is the number density of bubbles. N and d can be determined from video microscopy images and r_e and θ_c have been previously determined from etch rate and contact angle measurements [18]. For typical etching values in 2 M KOH ($N = 20\ \text{cm}^{-2}$; $r_e = 20\ \mu\text{m h}^{-1}$; $d = 1$ mm; $\theta_c = 42°$; $t = 2$ h) $\sigma_{(111)} = 0.019$ and therefore, approximately 2% of the total (1 0 0) surface area is transformed into (1 1 1) facets after 2 h etching. This would correspond to the formation of 5.9×10^7 pyramids per cm^2 each having a height of 0.1 μm. However, the size of bubble-induced pyramids is expected to be even larger since they grow continuously once formed, up to a size of approximately 1–2 μm. The detailed mechanism by which bubble imprints are transformed into pyramids is not clear but it can be assumed that surface features formed by overlapping bubble imprints constitute the nuclei for the formation of micro-pyramids. Thus, the above calculation shows that bubbles contribute significantly to the surface roughness and hence to micro-pyramid formation.

The size dependant nature of bubble imprints should be discussed in the context of bubble-induced defect formation. On n-Si(1 0 0), hydrogen bubbles create depressions with $d < 100$ μm and plateaux with $d > 100$ μm (Fig. 7). The depressions caused by small bubbles at an early stage of bubble growth (about 60 nm deep) should lead to significant surface roughness also at high KOH concentration and/or positive potentials, but this is not observed. The reason for this apparent discrepancy could be that an etch rate maximum in 6 M KOH is already reached in the absence of a thin layer of aqueous KOH and hence an increase of c_{KOH} in the thin layer does not lead to the formation of depressions.

From the above analysis, it is evident that the bubble-induced roughening of the sample dominates when large bubble sizes prevail. The observation that the surface roughness is drastically reduced when etching is performed under ultrasound [18], where bubbles are detached at an early stage of growth, strongly supports this proposal. It is concluded that surface termination is the most important factor determining roughness.

3.6. Estimation of the steady-state height of micro-pyramids

For practical applications, it is desirable to estimate the average height of pyramidal protrutions during anisotropic etching. The steady-state surface condition must take into account the rates of birth, growth and death of pyramids and several models describing the genesis and the time evolution of pyramidal hillocks have been recently developed [2,44–46]. In addition, Monte-Carlo simulations have been successfully used to model structure formation and mask under-etching in micromachining [47]. These studies did not take into account the influence of bubble adhesion and a simple qualitative discussion taking into account these effects is presented below.

The stability of the pyramidal hillocks is probably related to the presence of slow etching Si(1 1 1) planes limiting the pyramid sides [7,48–51]. In what follows the etching surface is modelled considering a (1 0 0) surface exposing (1 1 1) planes [52] (see Fig. 8d and e). This basic structure corresponds to the AFM images shown in Fig. 8c. From geometrical considerations, the average change in pyramid height, $\mathrm{d}\bar{h}/\mathrm{d}t$, can be expressed in terms of the etch rates of the Si(1 1 1), $r_{(111)}$, and the Si(1 0 0), $r_{(100)}$, planes:

$$\frac{\mathrm{d}\bar{h}}{\mathrm{d}t} = -1.73 r_{(111)} + r_{(100)} + \left(\frac{\partial \bar{h}}{\partial t}\right)_{R_{\text{dis}}} \quad (7)$$

The first two terms in the right hand side of Eq. (7) represent the average height decrease due to the removal rate of the limiting pyramid planes. The factor 1.733 ($= \sin(30.25°) + \cos^2(30.25°)/\sin(30.25°)$) results from the

geometry of the etching plane. $(\mathrm{d}\bar{h}/\mathrm{d}t)_{R_{\mathrm{dis}}}$ represents the rate of formation of Si(1 1 1) planes due to various roughening processes. A qualitative description of the potential dependence of surface roughness given by Eq. (7) must take into account the dependence of the etch rate ($r_{(111)}$) on pyramid height (h) due to the formation of local cells between the electrochemically different surface planes [20,53]. If the rate of formation of Si(1 1 1) planes due to bubble adhesion increases, the roughness of the surface must also increase in order to increase the dissolution rate of the (1 1 1) planes to establish a new steady state ($\mathrm{d}h/\mathrm{d}t = 0$). If it is assumed that the ratio of the surface areas of Si(1 0 0) and Si(1 1 1) remains constant during the transition from smooth to rough surfaces, as seems to be justified from the images shown in Fig. 8, then surface roughening can be described by an increase of the absolute size (L) of the macroscopic unit cell at the surface as shown in Fig. 8d and e. Consequently, the size of pyramids has to increase when the formation rate of Si(1 1 1) planes increases and/or the dissolution rate of Si(1 1 1) planes decreases by a shift of the potential towards negative values with its concomitant increase of bubble adhesion. The same arguments can obviously be used to explain the increase of pyramid size and surface roughness when the KOH concentration is decreased from 6 to 2 M.

The simple model presented above explains qualitatively why the size of pyramids and hence the surface roughness, increases when the potential is shifted from the current peak region to more negative values. It also predicts a reversibility of the potential induced structural transition from a rough to a smooth surface, which is indeed experimentally observed. However, a quantitative calculation of the dependence of the surface roughness on etching parameters is difficult, even though the rate of formation of Si(1 1 1) planes due to bubble adhesion can be estimated as discussed in the previous section. The problem is that the dependence of $r_{(111)}$ on h, E, c_{KOH} and T is not known in detail and may depend on seemingly minor details of surface termination and surface geometry.

4. Summary

A quantitative analysis of the diameter and lifetime of hydrogen bubbles formed on Si(1 0 0) during etching in aqueous KOH has been carried out. It is shown that potential, temperature and KOH concentration have a pronounced influence on d and τ. At potentials positive of the OCP and/or at high KOH concentrations the size of the hydrogen bubbles is small ($d = 20$–$100\ \mu\mathrm{m}$). Under these conditions, defect-free etching with an rms surface roughness of just a few nanometers can be realised fairly independently of etch depth. With increasing negative potentials and/or at low KOH concentrations, the bubble lifetime and the bubble density on the etching surface increases greatly and formation of pyramidal hillocks is observed resulting in a surface roughness in the order of 1 μm under these more anisotropic etching conditions. In situ FTIR spectroscopy shows a pronounced decrease of surface hydrogen termination and the formation of new, more hydrophilic surface species when the KOH concentration and/or the potential are increased, which explains the strongly reduced bubble adhesion under these etching conditions.

A quantitative analysis of number density and diameter of hydrogen bubbles makes it possible to estimate the density of (1 1 1)-oriented planes induced by bubble adhesion. From this estimation it can be concluded that the presence of hydrogen bubbles on the etching surface is the predominant source of micro-pyramids and long-range roughness observed under highly anisotropic etching conditions. This conclusion is strongly supported by the observation that the surface roughness is drastically reduced if the etching is performed under ultrasound radiation. A simple, qualitative model of surface roughness is presented relating the occurrence of large micro-pyramids to the adhesion of hydrogen bubbles.

For applications of wet chemical etching of Si(1 0 0) in micromachining technology, where both a high anisotropic ratio and a good surface finish are of importance, it seems desirable to reduce the lifetime of hydrogen bubbles by agitation or ultrasound since chemical additives, such as oxidants, or etching at anodic potentials and/or at high KOH concentrations, although effective in reducing the surface roughness, also decrease the (1 0 0):(1 1 1) anisotropic etching ratio.

Acknowledgements

The support by the European Commission (FUPUSET project, Brite/EuRam BE97-4371) is gratefully acknowledged.

References

[1] D.B. Lee, Journal of Applied Physics 40 (1969) 4569.
[2] M. Elwenspoekm, H.V. Jansen, Silicon Micromachining, Cambridge University Press, Cambridge, 1999.
[3] S.D. Collins, Journal of the Electrochemical Society 144 (1997) 2242–2262.
[4] C.M.A. Ashruf, P.J. French, P. Bressers, P.M. Sarro, J.J. Kelly, Sensors and Actuators a—Physical 66 (1998) 284–291.
[5] M.J. Vellenkoop, A.J. van Rhijn, G.W. Lubking, A. Venema, Sensors Actuators A 25–27 (1991) 699.
[6] M. Hoffmann, P. Kopka, E. Voges, IEEE Journal of Selected Topics Quantum Electronics 5 (1999) 46.
[7] H. Seidel, L. Csepregi, A. Heuberger, H. Baumgärtel, Journal of the Electrochemical Society 137 (1990) 3612.
[8] D.L. Kendall, Annual Review of Materials Science 9 (1979) 373–403.
[9] Nexus Task Force, The European Commission, NEXUS (The Network of Excellence in Multifunctional Microsystems), 1998.
[10] E.D. Palik, O.J. Glembocki, I. Heard, Journal of the Electrochemical Society 134 (1987) 404–409.
[11] P. Allongue, V. Costa-Kieling, H. Gerischer, Journal of the Electrochemical Society 140 (1993) 1018.
[12] P.M.M.C. Bressers, S.A.S.P. Pagano, J.J. Kelly, Journal of Electroanalytical Chemistry 391 (1995) 159.
[13] O.J. Glembocki, E.D. Palik, G.R. De Guel, D.L. Kendall, Journal of the Electrochemical Society 138 (1991) 1055–1063.

[14] E.D. Palik, V.M. Bermudez, O.J. Glembocki, Journal of the Electrochemical Society 132 (1985) 871.
[15] S.A. Campbell, K. Cooper, L. Dixon, R. Earwaker, S.N. Port, D.J. Schiffrin, Journal of Micromechanics and Microengineering 5 (1995) 209–218.
[16] E.D. Palik, O.J. Glembocki, I. Heard, P.S. Burno, L. Tenerz, Journal of Applied Physics 70 (1991) 3291–3300.
[17] T. Baum, D.J. Schiffrin, Journal of Micromechanics and Microengineering 7 (1997) 338–342.
[18] T. Baum, J. Satherley, D.J. Schiffrin, Langmuir 14 (1998) 2925–2928.
[19] H. Schröder, E. Obermeier, A. Steckenborn, Journal of Micromechanics and Microengineering 9 (1999) 139–145.
[20] P. Raisch, W. Haiss, R.J. Nichols, D.J. Schiffrin, Electrochimica Acta 45 (2000) 4635–4643.
[21] W. Haiss, P. Raisch, D.J. Schiffrin, L. Bitch, R.J. Nichols, Faraday Discussion 121 (2002).
[22] A. Bewick, M. Kalaji, G. Larramona, Journal of Electroanalytical Chemistry 318 (1991) 207–221.
[23] S.A. Campbell, D.J. Schiffrin, P.J. Tufton, Journal of Electroanalytical Chemistry 344 (1993) 211.
[24] T. Baum, D.J. Schiffrin, Journal of the Chemical Society—Faraday Transactions 94 (1998) 691.
[25] J. Kwo, M. Hong, A.R. Kortan, K.L. Queeney, Y.J. Chabal, R.L. Opila, D.A. Muller, S.N.G. Chu, B.J. Sapjeta, T.S. Lay, J.P. Mannaerts, T. Boone, H.W. Krautter, J.J. Krajewski, A.M. Sergnt, J.M. Rosamilia, Journal of Applied Physics 89 (2001) 3920–3927.
[26] X.H. Xia, J.J. Kelly, Electrochimica Acta 45 (2000) 4645.
[27] O.J. Glembocki, R.E. Stahlbush, M. Tomkiewicz, Journal of the Electrochemical Society 132 (1985) 145–151.
[28] J.W. Faust, E.D. Palik, Journal of the Electrochemical Society 130 (1983) 1413.
[29] R.L. Smith, B. Kloeck, N. De Rooij, S.D. Collins, Journal of Electroanalytical Chemistry 238 (1987) 103–113.
[30] E.D. Palik, J.W. Faust, H.F. Gray, R.F. Greene, Journal of Electrochemical Society 129 (1982) 2051–2059.
[31] D. Lapadatu, R. Puers, Sensors and Actuators a—Physical 60 (1997) 191–196.
[32] X.H. Xia, J.J. Kelly, Physical Chemistry Chemical Physics 3 (2001) 5304–5310.
[33] L.E. Scriven, Chinese Engineering Science 10 (1959) 1–13.
[34] S.F. Jones, G.M. Evans, K.P. Galvin, Advances in Colloid and Interface Science 80 (1999) 27–50.
[35] C. Mazzara, J. Jupille, W.Q. Zheng, M. Tanguy, A. Tadjeddine, P. Dumas, Surface Science 428 (1999) 208–213.
[36] O.M.R. Chyan, J.J. Wu, J.J. Chen, Applied Spectroscopy 51 (1997) 1905–1909.
[37] E.P. Boonekamp, J.J. Kelly, J. Vandeven, A.H.M. Sondag, Journal of Applied Physics 75 (1994) 8121–8127.
[38] J. Rappich, H.J. Lewerenz, H. Gerischer, Journal of the Electrochemical Society 140 (1993) L187–L189.
[39] C.H. Bjorkman, M. Fukuda, T. Yamazaki, S. Miyazaki, M. Hirose, Japanese Journal of Applied Physics Part 1—Regular Papers Short Notes and Review Papers 34 (1995) 722–726.
[40] F. Ozanam, A. Djebri, J.N. Chazalviel, Electrochimica Acta 41 (1996) 687–692.
[41] Y.J. Chabal, Physica B 170 (1991) 447–456.
[42] G.J. Pietsch, Y.J. Chabal, G.S. Higashi, Surface Science 333 (1995) 395–401.
[43] P. Raisch, W. Haiss, R.J. Nichols, D.J. Schiffrin, Journal of Physical Chemistry B 105 (2001) 12508–12515.
[44] A.J. Nijdam, J.W. Berenschot, J. van Suchtelen, J.G.E. Gardeniers, M. Elwenspoek, Journal of Micromechanics and Microengineering 9 (1999) 135–138.
[45] L.M. Landsberger, S. Naseh, M. Kahrizi, M. Paranjape, Journal of Microelectromechanical Systems 5 (1996) 106–116.
[46] J.T.L. Thong, P. Luo, W.K. Choi, S.C. Tan, Journal of Micromechanics and Microengineering 11 (2001) 61–69.
[47] M.A. Gosalvez, R.M. Nieminen, P. Kilpinen, E. Haimi, V. Lindroos, Applied Surface Science 178 (2001) 7–26.
[48] H. Schröder, E. Obermeier, A. Steckenborn, Journal of Micromechanics and Microengineering 8 (1998) 99–103.
[49] D.L. Kendall, Applied Physics Letters 26 (1975) 195.
[50] P. Allongue, V. Costakieling, H. Gerischer, Journal of the Electrochemical Society 140 (1993) 1018–1026.
[51] I. Zubel, Sensors and Actuators a—Physical 70 (1998) 260–268.
[52] Although we refer to the (111) plane, other high index planes may be exposed.
[53] P. Raisch, PhD thesis, Department of Chemistry, University of Liverpool, Liverpool, 2001, p. 189.